# Azimuthal motion of the mean wind in turbulent thermal convection

Heng-Dong Xi, Quan Zhou, and Ke-Qing Xia
*Department of Physics, The Chinese University of Hong Kong, Shatin, Hong Kong, China*
(Received 20 February 2006; published 26 May 2006)

We present an experimental study of the azimuthal motion of the mean wind in turbulent thermal convection. The experiments were conducted with cylindrical convection cells of unity aspect ratio and over the range of the Rayleigh number from $1\times10^9$ to $1\times10^{10}$. The azimuthal angle of the circulation plane of the mean wind was measured using both the particle image velocimetry and flow-visualization techniques. It is found that the azimuthal motion consists of erratic fluctuations and a time-periodic oscillation. The orientation of the wind is found to be "locked," i.e., it fluctuates about a preferred direction most of the time with all other orientations appearing as "transient states," and large excursions of the azimuthal angle often result in a net rotation which takes the wind back to the preferred orientation. The rate of erratic rotation of the circulation plane is found to have a strong dependence on Ra. Our result suggests that the oscillatory motion of the wind in its vertically oriented circulation plane and the orientational oscillation of the circulation plane itself have the same dynamic origin.

DOI: 10.1103/PhysRevE.73.056312 PACS number(s): 47.27.Jv, 47.27.te, 05.65.+b, 47.55.P−

## I. INTRODUCTION

We consider fluid motion in a Rayleigh-Bénard convection cell, a box with thermally conducting top and bottom plates and insulating sidewall that is heated from below and cooled on the top. The fluid is set to motion when the applied temperature difference exceeds a critical value. The dynamics of the flow is determined by the geometry of the cell and two dimensionless parameters: the Rayleigh number $\mathrm{Ra}=\alpha g\Delta L^3/(\nu\kappa)$ and the Prandtl number $\mathrm{Pr}=\nu/\kappa$, where $\Delta$ is the applied temperature difference, $L$ is the height of the cell, $g$ is the acceleration due to gravity, and $\alpha$, $\nu$, and $\kappa$ are, respectively, the volume expansion coefficient, kinematic viscosity, and thermal diffusivity of the fluid. Turbulent Rayleigh-Bénard convection has attracted a lot of interest during the past decade partly due to its relevance to astrophysical and geophysical phenomena such as solar and mantle convections [1,2].

At sufficiently high values of Ra, a large-scale circulation, in the form of a single roll comparable to the size of the convection cell, emerges [3–5]. The various aspects of this large-scale circulation (LSC), also known as the "mean wind" in turbulent convection, has been studied extensively over the years, using both experimental and numerical/theoretical approaches. These include its boundary layer properties [6–18], the scaling of its speed with Ra, Pr, and the geometry of the convection box [19–29], and its spatial structure and flow dynamics [30–47]. Through these studies, it is now generally believed that the flow dynamics in the circulation plane of the mean wind may be described by a flywheel structure which was proposed by Kadanoff [2] and Zocchi *et al.* [48]. In this picture, the laterally separated warm and cold plumes rise and fall in the two opposing sidewall regions in a synchronized fashion and drive the bulk fluid in the cell interior [34,37,39,41,49]. In a recent experimental study of the onset properties of the wind, Xi *et al.* [50] confirmed that the thermal plumes are indeed responsible for its formation and sustenance.

From the cylindrical symmetry of the convection cell (which is the most widely used geometry), one would expect that the dominant flow structure would have the same symmetry as the cell, such as hot fluid rise in the center and cold fluid fall along the periphery. Clearly the single circulatory-roll structure of the wind is not a stable flow mode for the geometry of the convection cell and one would expect the circulation plane of the wind to wander azimuthally. Because of the limitations in experimental techniques, systematic investigations of this azimuthal motion of the wind have been made only very recently [31,42,51,52]. Another related feature of the wind is the apparent random reversal of its circulation direction [31,53–55]. In addition to its importance in understanding the dynamics of turbulent flow in the Rayleigh-Bénard system, the putative connection of this phenomenon to similar reversals in the magnetic polarity of the earth [56,57] and in the wind direction in the earth's atmosphere [58] also makes it to be of more general interest. As a result, there have been quite a few experimental and theoretical studies devoted to this phenomenon in recent years [51,53,54,59–61]. For example, Sreenivasan *et al.* have made detailed analyses of the statistical properties of the observed reversal events and found that the reversals possess features of self-organized criticality. They also proposed a physical model to explain their findings [54,55]. Because of the nature of the experimental techniques used, the switching of the flow direction observed in [53–55] is consistent with both a fast 180° azimuthal rotation of the circulation roll and an in-plane reversal of the wind direction that requires a momentary vanishing of the wind speed, a cessation, before the directional change. This latter scenario is the one that has been considered in several recent model studies [60,61]. In a recent experiment, Brown *et al.* studied the orientational motion of the wind using multiple temperature probes and showed that both types of events indeed exist, but reversals involving a cessation are much rarer compared to reversals due to azimuthal rotation [51]. More recently, Hwa *et al.* have found that the intervals of wind reversal exhibit properties of critical fluctuations found in systems near the criti-

 

cal point of phase transitions [62]. Another issue of interest is how the bulk oscillations observed in the largely vertically oriented circulation plane [41] and the oscillation of plume orientations observed near the conduction plates [63] are related to each other. The former oscillation is now believed to be caused by the synchronized emission of the thermal plumes from the top and bottom plates [39,41], while the origin for the latter remains unclear.

In this paper, we report an experimental study of the azimuthal motion of the mean wind. Particle image velocimetry (PIV) technique and a flow visualization method have been used in the study. Both methods give a quantitative measure of the azimuthal angle of the wind; the PIV in addition measures its circulating speed. The experiments were made in cylindrical convection cells of aspect ratio $\Gamma=1$ using water as the working fluid. It is found that the azimuthal motion is a superposition of a periodic oscillation and erratic fluctuations. The apparently stochastic azimuthal motion generates a net-rotation on average.

The remainder of the paper is organized as follows. We describe the convection cells and experimental methods in Sec. II. The experimental results will be presented and discussed in Sec. III, which consists of five subsections. In Sec. III A, we present the overall features of the time trace of the measured azimuthal angle. Section III B discusses two particular types of events, rotations and cessations, that lead to the reversal of the flow direction. The time-periodic oscillations of the azimuthal angle and its relation to the wind speed are discussed in Sec. III C. In Sec. III D we discuss the properties of the so-called residence phenomenon. In Sec. III E we study the statistical properties of a special type of rotation event that leads to switching of the flow direction near the sidewall and can thus be classified as a reversal event. We summarize our findings and conclude in Sec. IV.

## II. EXPERIMENT

### A. The convection cells

Two cells were used in this experiment and water was the convecting fluid in both cases. The first one, used in the PIV measurement, consists of a sapphire disc as top plate and a copper disc as bottom plate. A schematic diagram of the cell is shown in Fig. 1. Starting from the top is a flat Plexiglas disc (A) and a stainless steel ring (B) of height 2.9 cm which, together with the sapphire disc (C) of diameter 19.5 cm and thickness 5.0 mm (Almaz Optics Inc.), form a cooling chamber. Two rubber o-rings (not shown) are used to provide seals between the sapphire plate and the steel ring and between the ring and the Plexiglas disc. A refrigerated circulator is connected to the cooling chamber via four nozzles (D). The temperature stability of the refrigerated circulator is 0.01 °C. The sidewall is a Plexiglass tube (E) of inner diameter 18.5 cm and wall thickness 8 mm. The bottom copper plate (F) is 1.4 cm thick and coated with a thin layer of nickel. The distance between the top and bottom plates is 18.5 cm, so the aspect ratio $\Gamma$ of the cell is 1. Two thin-film resistive heaters (G) connected in series are sandwiched between the bottom plate and a stainless steel bottom cover (H). The heaters are connected to a dc power supply

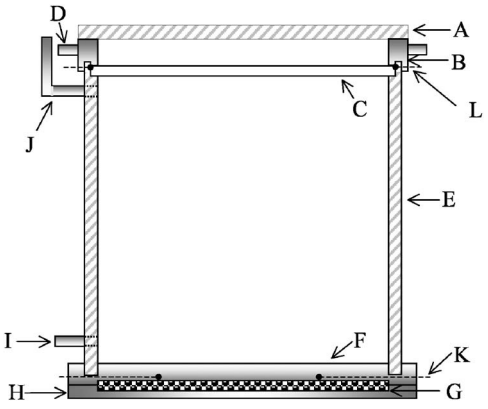


FIG. 1. A schematic drawing of the convection cell used in the PIV measurement. The top plate of the cell is made of sapphire so that flow in a horizontal plane can be visualized and measured. See text for a description of the legends.

with 99.99% long-term stability (Xantrex XFR 300-4). Draining (I) and filling (J) tubes are fitted on the sidewall at a distance of 1.5 cm from the top and bottom plates, so that they will not interfere with the light-sheet used in the PIV measurements near the boundary layer. Four thermistors (K and L) (Omega Engineering, Inc.), two in each plate, are used to monitor the temperature of the plates. It was found that the measured relative temperature difference between the two thermistors in the same plate was less than 1% for both plates for all Ra. This indicates that the temperature is uniform across the horizontal plates.

In the visualization measurement, a second cell with top and bottom plates both made of copper was used. The cell has been described in detail previously [16,64]. We outline only its main features here. The copper plates have thickness of 1 cm and are plated with a thin layer of nickel. A stainless steel cover is attached on the top of the upper plate. This cover together with the upper surface of the top copper plate serves as a cooling chamber, which removes heat from the top surface via a refrigerated circulator. Cold water is pumped to the chamber through two inlets and flows out through two outlets on the top of the chamber. Two silicon rubber film heaters connected in series are sandwiched to the backside of the bottom plate to provide constant and uniform heating. The sidewall is a Plexiglass cylinder of 19 cm inner diameter and 5 mm thickness. The distance between the two plates is 19 cm so that the aspect ratio $\Gamma$ is also unity.

### B. The PIV measurement

The particle image velocimetry (PIV) technique is used to measure the two-dimensional (2D) horizontal velocity field near the top plate of the sapphire convection cell. The PIV system consists of a dual Nd:YAG laser operated at a power of 80 mJ per pulse, light-sheet optics, a cooled CCD camera with 12-bit dynamic range and $1280\times1024$ spatial resolution, and a synchronizer and control software, which contains a PIV data analysis package. During the measurement, a laser light-sheet of thickness $\simeq 2$ mm is used to illuminate the seed particles in a horizontal plane of the cell. The mea-

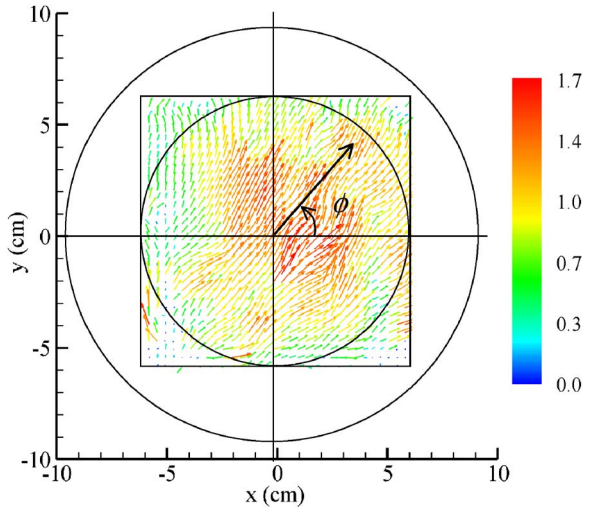


FIG. 2. (Color online) An instantaneous vector map of the measured velocity field in a horizontal plane near the top plate of the convection cell ($Ra=3.0\times10^9$). The velocity magnitude is coded in both color and the size of the arrow and the boundary of the measuring area is indicated by the square. The large circle represents the horizontal cross section of the cell, and the small circle indicates the area of spatial average for the orientation vector $\mathbf{V}_{LSC}$ (the large black arrow).

suring area is a square of $12\times12$ cm$^2$ at the center of the plate. Each 2D velocity vector is calculated from a subwindow ($32\times32$ pixels) that has 50% overlap with its neighboring subwindows [65]; this gives $63\times63$ velocity vectors for the measured velocity field, or vector map. The corresponding spatial resolution is 1.9 mm. The seed particles used in the experiment are 10 $\mu$m diameter polyamid spheres (density=1.03 g/cm$^3$). The selection criteria for the size of the seed particles and for the operating parameters such as pulse separation time have been described in detail in Refs. [37,41] and thus will not be restated here.

Measurements were made in a plane 6 mm below the top plate, where the horizontal velocity is maximum as found by previous velocity measurement made in a vertical plane [41]. During the measurement the convection cell was leveled to within 0.2°. Figure 2 shows an instantaneous vector map measured by the PIV. The large circle in the figure represents the horizontal cross section of the cell. For clarity the figure is coarse grained by combining every four neighboring vectors into one and the velocity magnitude is coded both by color and by the length of the arrow. To study the azimuthal motion of the LSC, we define a velocity, which may be called the orientational vector, $\mathbf{V}_{LSC}$ to represent the overall direction and magnitude of the velocity field in the horizontal plane, $\mathbf{V}_{LSC}(t)=V_x(t)\hat{i}+V_y(t)\hat{j}$, where $V_x$ and $V_y$ are respective spatial averages of the local velocity components $v_x(t)$ and $v_y(t)$ measured by the PIV. The small circle (diameter 12 cm) in Fig. 2 indicates the area of spatial averaging, i.e., all velocity vectors contained inside the circle are included in the calculation of $\mathbf{V}_{LSC}$. A total of 3205 velocity vectors are contained in this area. The use of a circular area ensures that the number of velocity vectors used in the average is a constant in each direction irrespective of the azimuthal angle of the

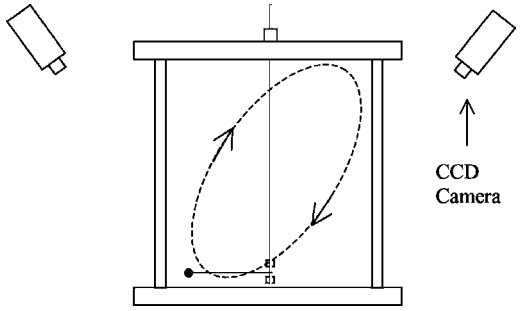


FIG. 3. A schematic drawing of the setup of the visualization measurement.

LSC. Circles with diameters of 4, 8, and 12 cm have been used and the square measuring area itself has also been used as the averaging region. The obtained results are essentially the same in all cases. From the orientational vector $\mathbf{V}_{LSC}$ we obtain the speed or magnitude of the mean wind $V_{LSC}\equiv|\mathbf{V}_{LSC}|=(V_x^2+V_y^2)^{1/2}$ and the azimuthal orientation of the circulation plane of the wind $\tan\phi=V_y/V_x$. The azimuthal angle $\phi$ of the wind is defined as the angle between $\mathbf{V}_{LSC}$ and the $x$ axis (see Fig. 2). Here $\phi$ is defined as a continuous variable, i.e., it could be larger than 360° or less than 0°, and anticlockwise is defined as positive when looked from top. The thick arrow in Fig 2 represents $\mathbf{V}_{LSC}$ for the given instantaneous velocity field. It is seen that the direction of $\mathbf{V}_{LSC}$ corresponds to the overall direction of the individual velocity vectors of the underlying flow field and is thus a very good representation of the azimuthal orientation of the wind.

### C. The flow-visualization measurement

To study the long-term trend and certain statistical properties of the azimuthal motion, the PIV method becomes unpractical. So a flow-visualization measurement was made. The azimuthal motion of the mean wind is visualized and measured by a styrofoam bead (diameter$\approx$1 mm) attached to fishing lines (diameter=0.18 mm). The densities of the bead and the fishing line are such that the assembly is neurally buoyant in the fluid. As shown in Fig. 3 the assembly is loosely reeled on a small stainless steel tube at the central axis of the cell and near the bottom plate. The bead is located at a distance of approximately 2 cm from the sidewall so that it is not sensitive to the predominantly vertical flows near the sidewall; rather, it follows the predominantly horizontal flows near the plates and thus indicates the orientation (or the azimuthal angle) of the vertical circulation plane of the LSC. Several fluorescence lamps are used to illuminate the bead. Four CCD cameras (Sony SPT-M128CE) were used to record the motions of the bead; each covers a 90° azimuthal angular region. Outputs from the CCDs were recorded in video format at a rate 0.67 frame/second and stored in a computer. The recorded video is converted into individual image files frame by frame and a program written in IDL is then used to automatically identify the position of the bead in each image, which gives azimuthal angle $\phi$ of the circulation plane of the LSC. It is estimated that the uncertainty in the measured $\phi$ is about 1.3°. To eliminate the influence of room

TABLE I. Experimental conditions of the seven runs; number of cessations and double cessations observed from the PIV measurement, and the phase delay between the absolute value of the azimuthal rotation rate $|\dot{\phi}|$ and the magnitude of the mean wind $V_{LSC}$.

| Run no. | Ra | Pr | Duration (h) | No. of cessations | No. of double cessations | Phase delay (s) |
|---|---|---|---|---|---|---|
| 1 | $1.0\times10^9$ | 5.3 | 120 | 1 | 0 | 0.29 |
| 2 | $3.0\times10^9$ | 5.3 | 57 | 1 | 0 | −0.70 |
| 3 | $4.7\times10^9$ | 5.4 | 56 | 1 | 0 | −0.96 |
| 4 | $6.5\times10^9$ | 5.3 | 72 | 3 | 2 | −0.83 |
| 5 | $9.7\times10^9$ | 4.8 | 33 | 7 | 2 | −0.47 |
| 6 | $1.05\times10^{10}$ | 4.6 | 58 | 9 | 2 | −0.76 |
| 7 | $6.5\times10^9$ | 5.3 | 783 | NA | NA | NA |

temperature fluctuations, the convection cell and the CCDs were kept in a thermostat box that has a temperature stability of better than 0.05 °C.

## III. RESULTS AND DISCUSSION

We now present and discuss the experimental results. Results presented in Secs. III A–III C are mainly from the PIV measurement, while those presented in Secs. III D and III E come from the flow-visualization measurement.

### A. Gross features of the azimuthal motion

The PIV measurement were made for six values of Ra, these were labeled as run nos. 1 to 6. The values of Ra, Pr, and measurement duration for these runs are listed in Table I, respectively. The sampling rates for these runs vary from 0.3 to 0.8 Hz and the acquired vector frames range from 70 000 to 200 000. Figure 4 plots the time trace of $\phi$ (in units of $2\pi$) from the six runs (note that the scales of both the horizontal and vertical axes are different for different panels of the figure). The first striking feature of these traces is the existence of the plateau levels in $\phi$. Note that the plateaus differ from each other by integral multiples of $2\pi$ so that they correspond to the same physical orientation of the circulation plane of the wind. Hence, these results show that the orientation of the wind fluctuates about a preferred direction for most of the time (>95% of the time) and sometimes undergoes a "fast" 360° turn at irregular intervals; here "fast" is in the sense of the time scale of hours. The fact that the orientation of the wind has a preferred direction has been reported previously by Cioni *et al.* [31] and more recently by Sun *et al.* [41] and Brown *et al.* [51]. But what was not found before is that the wind is essentially "locked" in the preferred direction. Nevertheless, as we will show in Sec. III E below, our results share certain statistical properties found in some of the previous studies.

Another feature revealed by these traces is that for larger Ra ($\geqslant 6\times10^9$) the rate of net rotation (clockwise in this case) is increased significantly. Net rotation of the circulation plane of the wind has been observed recently by Sun *et al.* in a $\Gamma=0.5$ cell and it appears to possess the characteristics of a Brownian ratchet [42]. Net rotation is also observed by

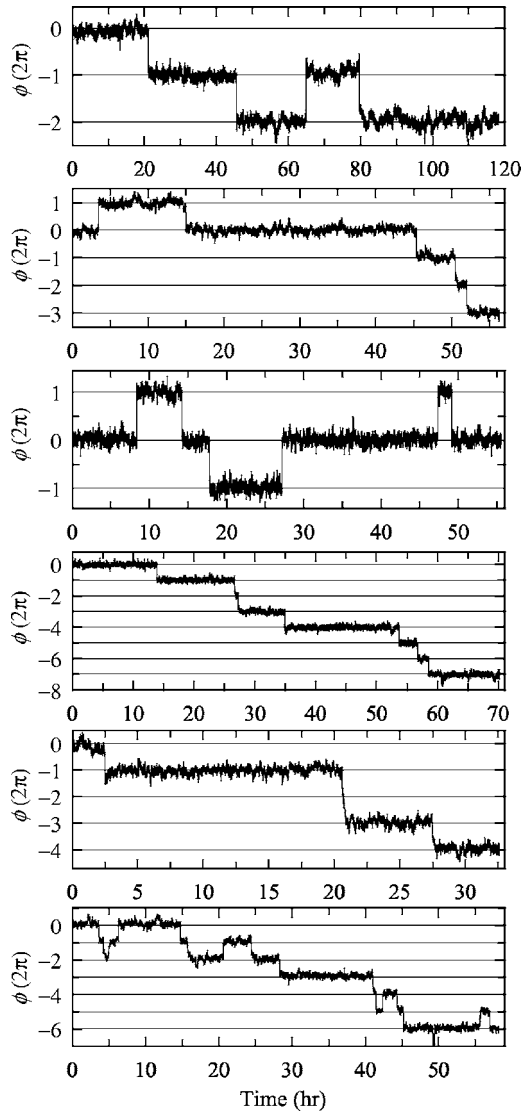


FIG. 4. Time series of the azimuthal orientation angle $\phi$ of the mean wind measured by the PIV. The Rayleigh numbers are, from top to bottom, Ra=$1.0\times10^9$, $3.0\times10^9$, $4.7\times10^9$, $6.5\times10^9$, $9.7\times10^9$, and $1.05\times10^{10}$.

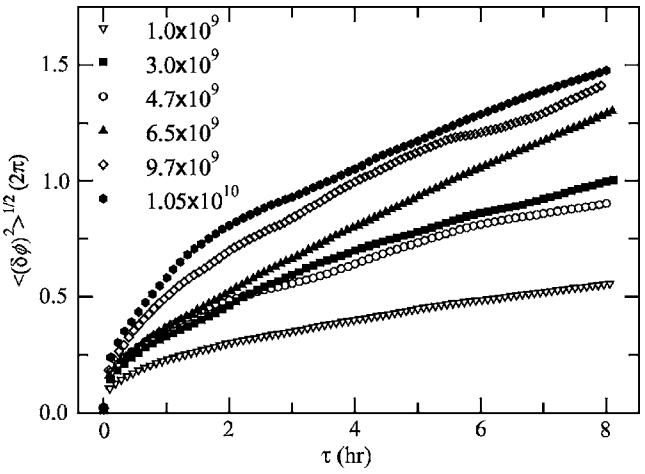


FIG. 5. Mean-square angular displacement $\langle(\delta\phi(\tau))^2\rangle^{1/2}$ as a function of $\tau$ (in units of $2\pi$) for all six values of Ra.

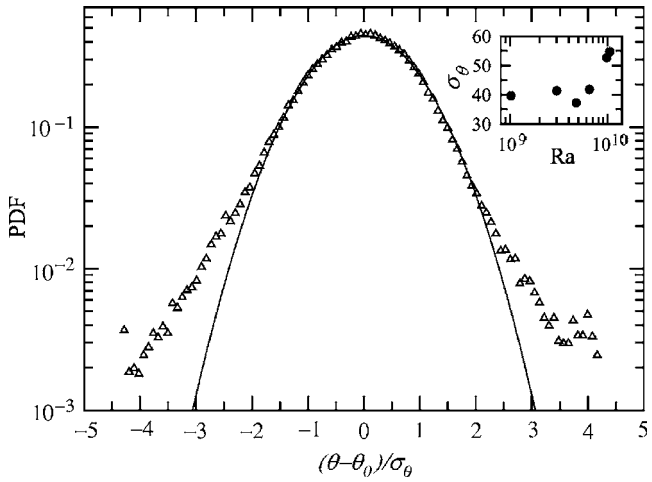


FIG. 6. The probability density function of $\theta$ of the physical azimuthal angle of the mean wind ($\mathrm{Ra}=6.5\times10^9$). The solid curve indicates a Gaussian distribution of the same standard deviation as the data. Inset: the standard deviation $\sigma_\theta$ (in units of degrees) of $\theta$ vs Ra.

Brown *et al.* [51] in a $\Gamma=1$ cell. But the rotation rate reported in [51] appears to be much slower ($\sim$1 revolution per day) than what is observed here. A statistical measure of the average time it takes the wind to change the orientation of its vertical circulation plane by a certain angle is the root mean square angular increment $\langle[\delta\phi(\tau)]^2\rangle^{1/2}$, where $\delta\phi(\tau)\equiv\phi(t+\tau)-\phi(t)$. Figure 5 plots $\langle[\delta\phi(\tau)]^2\rangle^{1/2}$ as a function of $\tau$ for the six Ra, which shows that the mean rotation rate increases rapidly with Ra. For example, on average, at $\mathrm{Ra}=1\times10^{10}$ it takes less than an hour for the wind to change its orientation by half of a revolution, whereas at $\mathrm{Ra}=1\times10^9$ the same change takes about 8 h to complete.

For ease of discussion, we introduce the physical azimuthal angle $\theta$ of the wind, which is defined as $\theta=\phi\pm2n\pi$, where $\theta$ is defined with respect to the $x$ axis (see Fig. 2) with counterclockwise as the positive direction and $n$ is an integer so chosen such that $-\pi\leqslant\theta<\pi$ (note that $n$ is not the number of net revolutions). Figure 6 shows the probability density function of $(\theta-\theta_o)/\sigma_\theta$ for $\mathrm{Ra}=6.5\times10^9$, where $\theta_o$ is the angle of the preferred orientation of the wind and the solid curve is a fitting of Gaussian distribution to the data with a standard deviation $\sigma_\theta\simeq42°$. This result shows that the distribution of $\theta$ is approximately Gaussian for small amplitude fluctuations about a preferred direction, but for fluctuations larger than about $2\sigma_\theta$ the probabilities are larger than those given by the Gaussian distribution and have exponential-like tails. The PDFs for other data sets show similar properties, with the values of $\sigma_\theta$ all around 40° except for the two highest Ra (see the inset of Fig. 6).

Regarding the preferred orientation $\theta_o$ of the wind, we do not find an obvious correlation between $\theta_o$ and any particular features of the convection cell, such as the location of the water inlet and outlet. On the other hand, the distribution of $\theta_o$ does not appear to be entirely random either. This is shown in Fig. 7, in which the arrows indicate the flow direction near the top plate. It shows that $\theta_o$ for all runs spanning an angular region of about 180°. Obviously, more systematic investigations are needed before any definitive statement about $\theta_o$ can be made.

To study the azimuthal motion of the wind in more detail, we examine the behavior of $\phi$ over different time scales. This is illustrated in Fig. 8 for $\mathrm{Ra}=6.5\times10^9$, in which the top panel reproduces the trace already shown in Fig. 4. The panels (b), (c), and (d) with expanded time scales reveal that there are several time scales imbedded in the apparent erratic fluctuations of $\phi$. First there appears to be an undulation over the time scale of several tens of minutes [(b) and (c)], but it is very irregular and does not show up as a peak in the power spectrum or autocorrelation function of $\phi$. It is also seen from these traces that even when the overall orientation of the mean wind appears to be locked in the preferred direction, i.e., $\phi$ fluctuates with "small amplitude" about a given plateau level, some of these erratic excursions can be larger than 90°. As will be discussed in Sec. III E, these larger than 90° fluctuations (or rotations) from the preferred direction

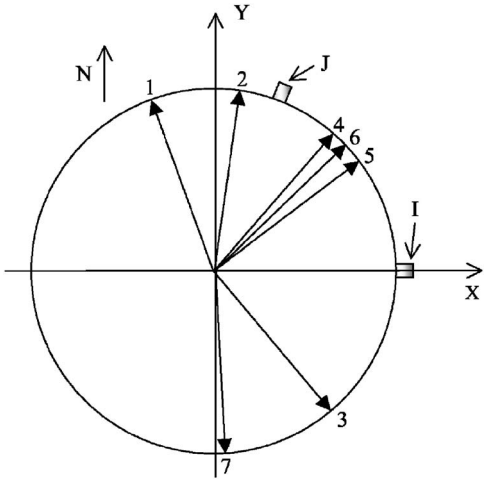


FIG. 7. A schematic top view of the cell indicating the preferred orientation of the mean wind for all seven runs; here the preferred azimuthal angle $\theta_o$ is represented by the black arrows which are labeled by the corresponding run numbers. The letter "N" indicates the geographical north. The positions of the draining (I) and filling (J) tubes are also indicated (see Fig. 1).

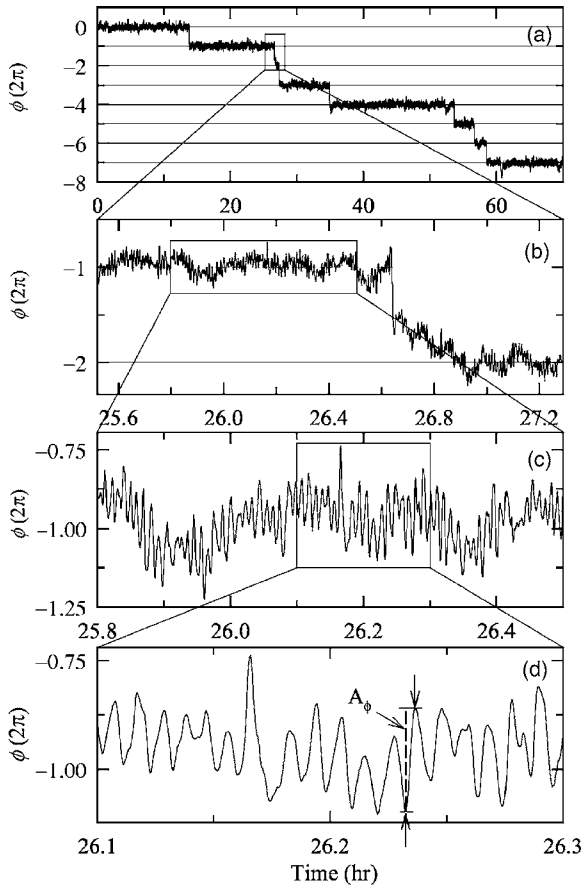


FIG. 8. Expanded views of the time trace of the azimuthal angle $\phi(t)$ of the mean wind (Ra=$6.5\times10^9$): (a) the entire trace of 72 h; (b) a segment of 108 min; (c) a segment of 42 min; and (d) a segment of 12 min.

will result in directional reversals of the vertical velocity component measured near the sidewall. Over the time scale of $\sim$1 min, $\phi$ displays a rather periodic oscillation [(c) and (d)]. We denote the period of this oscillation as $\tau_o$. As will be shown below, for the same Ra $\tau_o$ has the same value as the circulation time or turnover time of the mean wind measured in a vertical plane [41].

Figure 9 shows the power spectrum density of $\theta$ for the six PIV measurements, where the frequency has been scaled by the Ra-dependent turnover time $\tau_o$. The prominent peak indicates a time-periodic oscillation with a frequency $1/\tau_o$. This frequency agrees well with the circulation frequency of the wind obtained from both temperature and velocity measurements for comparable values of Ra and Pr [66,67]. It also corresponds to the oscillation frequency of the bulk fluid [41]. We believe that the oscillation in the orientation of the mean wind, superposed on top of an apparently erratic motion over longer time scales, should be the same motion observed by Funfschilling and Ahlers [63] in a shadowgraphic study in which it is identified as the oscillatory motion of thermal plumes. Because the mean wind is dominated by thermal plumes, it is not surprising that thermal measurement in [63] and direct velocity measurement here give the same result. Figure 9 also shows that at low frequencies the power spectrum has a roll-off rate of 2.0, suggesting that the erratic

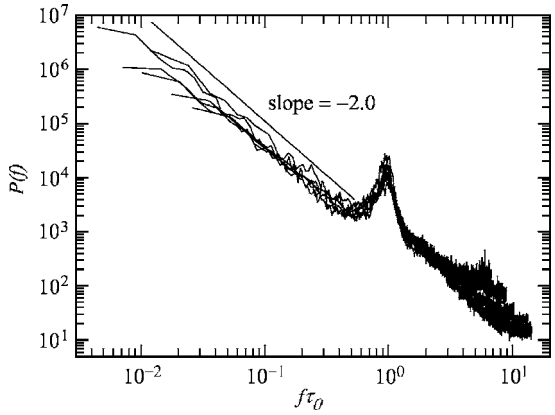


FIG. 9. Power spectrum density functions of $\phi$ for all the six values of Ra. Note that the horizontal axis is scaled by the turnover time $\tau_0$ of the flow, which is Ra dependent.

azimuthal motion of the mean wind over time scales longer than the periodic oscillation has characteristics of a Brownian process.

### B. Rotations and cessations

We now examine the dynamic behavior of $\phi$ together with the corresponding value of $V_{LSC}$, the speed of the mean wind. Figure 10 shows two examples of rotations; the left panel shows a "fast" rotation in which the LSC underwent a net azimuthal angular change of $\Delta\phi\simeq7/8$ (in units of $2\pi$) over a time interval of $\sim\tau_0$ and the right panel shows a "slow" rotation in which a net angular change of $\Delta\phi\simeq3/8$ took place over an interval of $\sim10\tau_0$. It is seen from the lower panel that $V_{LSC}$ remains nonzero during both events. We found that it takes anywhere from $\tau_0$ to $45\tau_0$ to complete a rotation of half a revolution, with the mean value being $15\tau_0$. Figure 11, on the other hand, shows different types of events than the above. The left panel shows that an angular change of about half a revolution occurred over a fraction of $\tau_0$. This is a cessation-led reversal as reported recently by Brown *et al.* [51]. From Fig. 11 one sees that, before any significant change of $\phi$ occurred, $V_{LSC}$ has decreased for

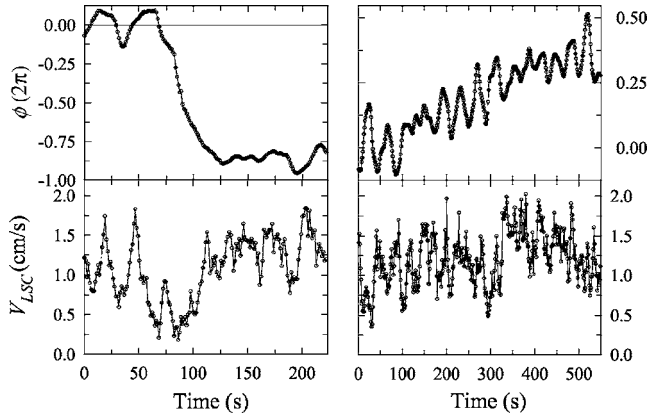


FIG. 10. The azimuthal orientation angle $\phi$ and the magnitude $V_{LSC}$ of the mean wind during fast (left panel) and slow (right panel) rotations.

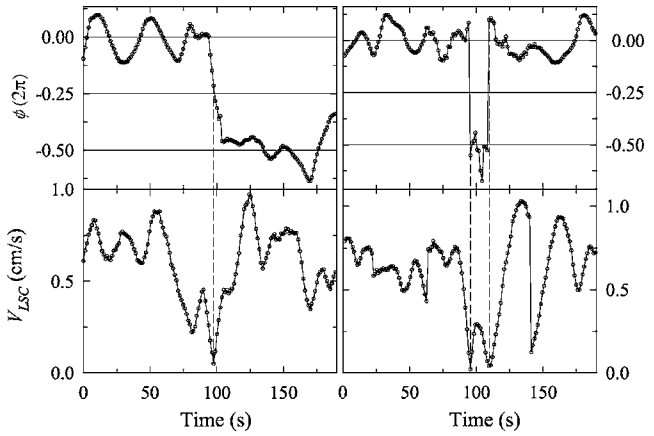


FIG. 11. The azimuthal orientation angle $\phi$ and the magnitude $V_{LSC}$ of the mean wind during cessation (left panel) and double cessations (right panel).

about half of a turnover time, it reached approximately zero during the reversal, and then increased for about another $0.5\tau_0$. It suggests that the mean wind gradually slowed to a stop, reversed its direction, and gradually sped up again without significant rotation of the wind's orientation. The right panel of Fig. 11 shows another type of event, which we call double-cessation. One sees that the orientation of the wind first changed by 180° over a fraction of $\tau_0$, while $V_{LSC}$ stayed approximately zero during the period. After less than half of $\tau_o$, the orientation underwent another very fast 180° change with $V_{LSC}$ again staying approximately zero. After the two reversals the wind returned to its previous orientation. Note that the entire duration of this double-cessation process is only about $0.5\tau_o$. It seems that double cessations are caused by the situation that whatever event that triggered the first cessation had insufficient energy to completely overturn the flow to the opposite direction, as a result the mean wind "stalled" and started again in the previous direction. The number of cessations and double cessations for the six data sets are listed in Table I. It is seen that cessation is indeed a very rare event. In Fig. 12 we show the distribution of angular change $|\Delta\phi|$ of the wind orientation in a cessation event. For the limited statistics, it is seen that the result may be considered as consistent with a uniform distribution, which is in agreement with the finding of [51].

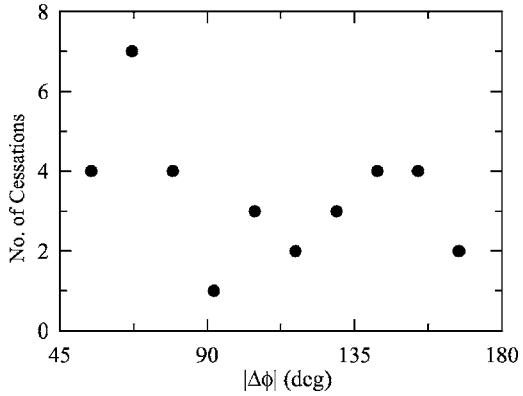


FIG. 12. The distribution of angular change $|\Delta\phi|$ of the wind orientation in a cessation event.

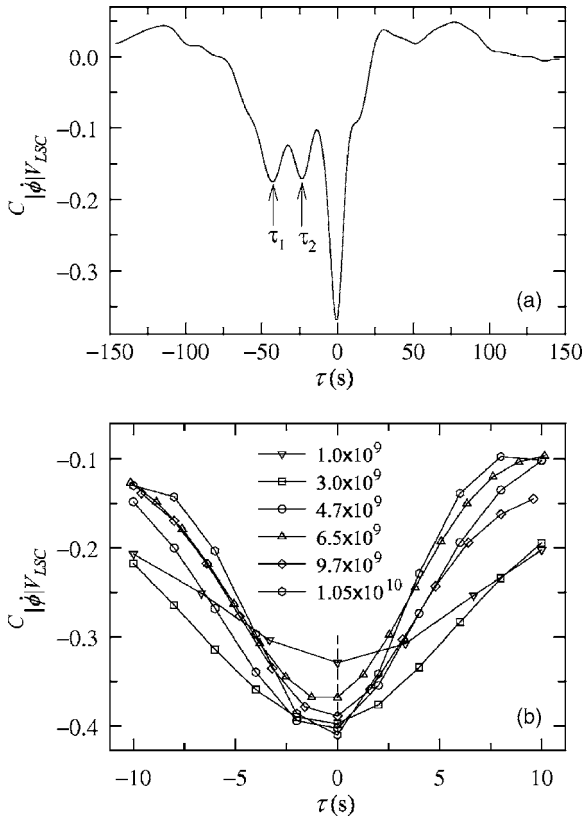


FIG. 13. (a) Cross-correlation function $C_{|\dot\phi|V_{LSC}}(\tau)$ between the absolute value of the azimuthal angular velocity $|\dot\phi|$ and the wind speed $V_{LSC}$ as a function of delay time $\tau$ (Ra=$6.5\times10^9$). (b) $C_{|\dot\phi|V_{LSC}}(\tau)$ near the main peak at $\tau=0$ for all six values of Ra.

From Fig. 11 we see that during a cessation event, the angular change is always proceeded by a sharp decrease in the wind speed. To study the general phase relationship between the orientational change and the speed of the wind, we examine the cross correlation between the absolute value of the azimuthal angular velocity $|\dot\phi|$ and the wind speed $V_{LSC}$,

$$C_{|\dot\phi|V_{LSC}}(\tau) = \langle[|\dot\phi(t+\tau)| - \langle|\dot\phi|\rangle][V_{LSC}(t) - \langle V_{LSC}\rangle]\rangle/(\sigma_{\dot\phi}\sigma_{V_{LSC}}),$$

where $\sigma_{\dot\phi}$ and $\sigma_{V_{LSC}}$ are standard deviations of $\dot\phi$ and $V_{LSC}$, respectively. Figure 13(a) shows $C_{|\dot\phi|V_{LSC}}(\tau)$ for Ra=$6.5\times10^9$. It shows that $|\dot\phi|$ and $V_{LSC}$ have a strong negative correlation with the main peak located at $\tau=0$. Negative correlation between the azimuthal rotation rate of the wind and its magnitude has been found previously by Brown *et al.* [51], but in addition they found that there is a phase difference between the two quantities with the wind amplitude leading the rotation rate by about 6% of the turnover time $\tau_o$. To examine our results in more detail, we plot in Fig. 13(b) an enlarged region near the main peak of $C_{|\dot\phi|V_{LSC}}(\tau)$ for all six data sets. It is seen that within experimental uncertainty all peak positions are indistinguishable from 0. In fact, when we fitted the exponential decay function used in [51] to our data, the obtained peak positions $\tau_p$ are within a fraction of a

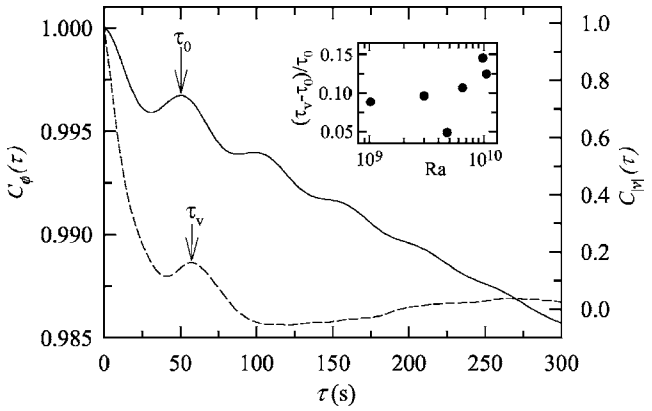


FIG. 14. Autocorrelation functions $C_\phi(\tau)$ of the orientation angle $\phi$ (solid line) and $C_{V_{LSC}}(\tau)$ of the magnitude $V_{LSC}$ (dashed line) as functions of delay time $\tau$.

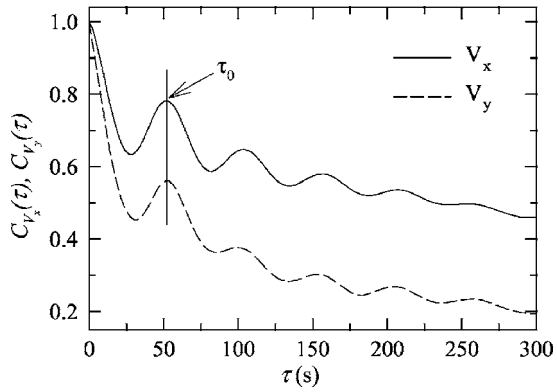


FIG. 15. Autocorrelation functions $C_{V_x}(\tau)$ (solid line) and $C_{V_y}(\tau)$ (dashed line) of the two horizontal velocity components of $\mathbf{V}_{LSC}$ as functions of delay time $\tau$.

second with no particular trend in their dependence on Ra. In column 7 of Table I we list the values of the phase delay $\tau_p$ for all six runs, which are negligibly small for the measurement uncertainty of the experiment. In contrast, over the same Ra range, the corresponding quantity in [51] decreases systematically with increasing Ra (from ~13.3 to 4.7 s). While we do not know the exact reason for this apparent discrepancy, we note that the measurements in [51] were at the mid-height of the convection cell and that the measured azimuthal angle does not exhibit periodic oscillations at that position, so that there could be a phase difference in the azimuthal rotation of the wind at the top and at mid-height. Another reason could be due to the different techniques used in the two experiments. In [51] temperature signals were used to indicate the motion of the wind, whereas direct velocity measurement was made in our case. While the wind is dominated by coherent thermal structures like plumes [48,50,68] so that temperature measurements can provide a good deal of information about the properties of the wind, it cannot be expected to give every detail of the velocity field. There is probably a limit to which results from direct velocity measurement and temperature measurement can be compared. It should be noted that our finding here does not contradict the results shown in Fig. 11 for the cessation events in which the wind speed $V_{LSC}$ is seen to indeed lead the angular change. This is because the few cessation events make a negligible contribution to the correlation function which is calculated from the entire time series and is thus dominated by the large number of random rotational events.

### C. The periodic azimuthal oscillation

We now discuss the two smaller peaks of $C_{|\dot\phi|V_{LSC}}(\tau)$ seen in Fig. 13(a), which are denoted as $\tau_1$ and $\tau_2$, respectively. We found that $\tau_1$ is very close to $\tau_0$ and $\tau_2$ is close to $\tau_0/2$. Clearly these time scales are related. To understand their origins we plot in Fig. 14 the autocorrelation functions of $\phi$ (solid line) and $V_{LSC}$ (dashed line), respectively. It is seen that the two quantities oscillate with periods that are very close to each other, but nonetheless different. The oscillation period of $\phi$ is just $\tau_0$ as found from its power spectrum. We label the oscillation period of $V_{LSC}$ as $\tau_v$. The inset of Fig. 14 shows the relative difference between the two periods for the different values of Ra and it is seen that the difference varies from ~5% to ~15%, but there is no clear trend with Ra. To understand this difference, recall that $V_{LSC}$ is derived from $V_x$ and $V_y$, i.e., $V_{LSC}=(V_x^2+V_y^2)^{1/2}$, where $V_x$ and $V_y$ are the spatial averages of the respective local velocity components measured by the PIV. Figure 15 plots the autocorrelation functions of $V_x$ and $V_y$ for the same Ra as in Fig. 14. It is seen that both $V_x$ and $V_y$ oscillate, within experimental uncertainty, with approximately the same period that are also approximately the same as that of $\phi$ (52.07, 51.77, and 52.00 s, respectively). It is also found that $V_x^2$ and $V_y^2$ oscillate with the same period as $V_x$ and $V_y$, but their sum $V_x^2+V_y^2$ has the same period as $V_{LSC}$ (57.3 s vs. 57.0 s). This implies that both the amplitude ($V_{LSC}$) and the azimuthal angle ($\phi$) of LSC velocity $\mathbf{V}_{LSC}$ oscillate, but with slightly different frequency. Also, the oscillation in $\phi$ is much stronger than the oscillation in $V_{LSC}$, which can be seen from their autocorrelation functions: $C_\phi(\tau)$ oscillates over many periods while $C_{V_{LSC}}(\tau)$ has only one oscillation peak. Because of this, the weak oscillation in $V_{LSC}$ is suppressed by the strong oscillation in $\phi$ in the components $V_x$ ($=V_{LSC}\cos\phi$) and $V_y$ ($=V_{LSC}\sin\phi$), but when their squares are added the dependence on $\phi$ is canceled and only the oscillation in $V_{LSC}$ remains. It is unclear how these two frequencies are related to each other, but their closeness and the fact that the two oscillations are in phase suggest that there is a single source or mechanism driving both oscillations.

The small peak with a delay time $\tau_1$ appearing in the cross-correlation function between $|\dot\phi|$ and $V_{LSC}$ shown in Fig. 13 may now be attributed to the fact that both $\phi$ (hence $\dot\phi$) and $V_{LSC}$ oscillate with roughly the same frequencies. The second small peak $\tau_2\simeq\tau_1/2$ may be understood from the "rectifying effect" arising from the use of the absolute value of $\dot\phi$ in the cross-correlation function. In Fig. 16 we plot the Ra dependence of the normalized frequencies corresponding to $\tau_0$, $\tau_1$, $\tau_2$, and $\tau_v$, which may be taken as equivalent to Peclét numbers. The solid lines in the figure represent power-law fits to the respective data: $L^2/(\kappa\tau_0)=0.084\mathrm{Ra}^{0.50\pm0.01}$, $L^2/(\kappa\tau_1)=0.215\mathrm{Ra}^{0.48\pm0.02}$, $L^2/(\kappa\tau_2)=0.115\mathrm{Ra}^{0.48\pm0.02}$, and

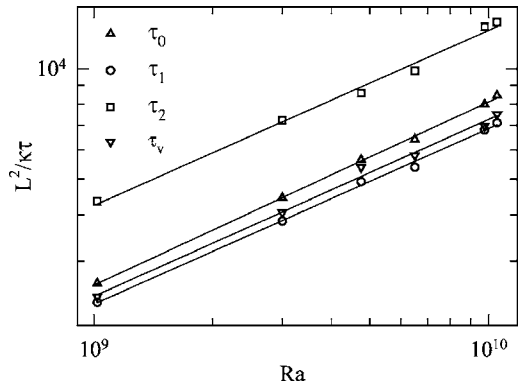


FIG. 16. Normalized oscillation period $L^2/\kappa\tau$ vs Ra for $\tau_0$, $\tau_1$, $\tau_2$, and $\tau_v$. See text for the explanations for the fitting lines.

$L^2/(\kappa\tau_v)=0.112\mathrm{Ra}^{0.48\pm0.02}$. Given the very limited range of Ra of the experiment, the values of the scaling exponent may be regarded as consistent with results from many previous measurements of the Reynolds number.

Finally, we examine the angular amplitude of the periodic oscillatory motion. This is done by identifying the local extrema in the measured time trace of $\phi$ (or $\theta$). An example is shown in the bottom panel of Fig. 8 where the difference between two neighboring extrema is taken as the amplitude of the periodic oscillation and denoted as $A_\phi$. The distribution of $A_\phi$ is shown in Fig. 17, which is seen to have a Gaussian-like distribution with a most probable value of 50°. The inset of Fig. 17 shows the average of $A_\phi$ for the six data sets. It is seen that $\langle A_\phi \rangle$ does to vary with Ra in any particular way, whereas the period $\tau_o$ of the oscillation has a well-defined scaling with Ra (see Fig. 16). Note that $A_\phi$ is essentially a subset of the physical angle $\theta$ (or $\theta-\theta_0$). Thus the distribution of $A_\phi$ suggests that Gaussian-like distribution for small values of $\theta-\theta_0$ as seen in Fig. 6 are mostly due to periodic oscillations and that the deviation from normality comes mainly from the erratic, nonperiodic part, of the azimuthal motion.

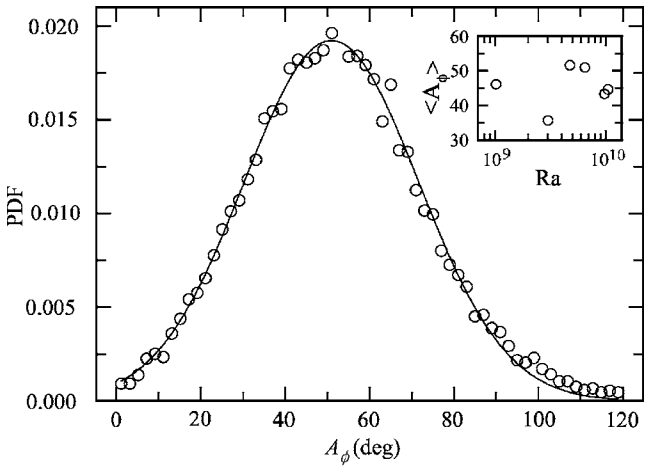


FIG. 17. Probability density function of the amplitude $A_\phi$ of the periodic oscillation for Ra=$6.5\times10^9$, with the solid curve indicating a Gaussian fit. Inset: the average of $A_\phi$ for the six values of Ra.

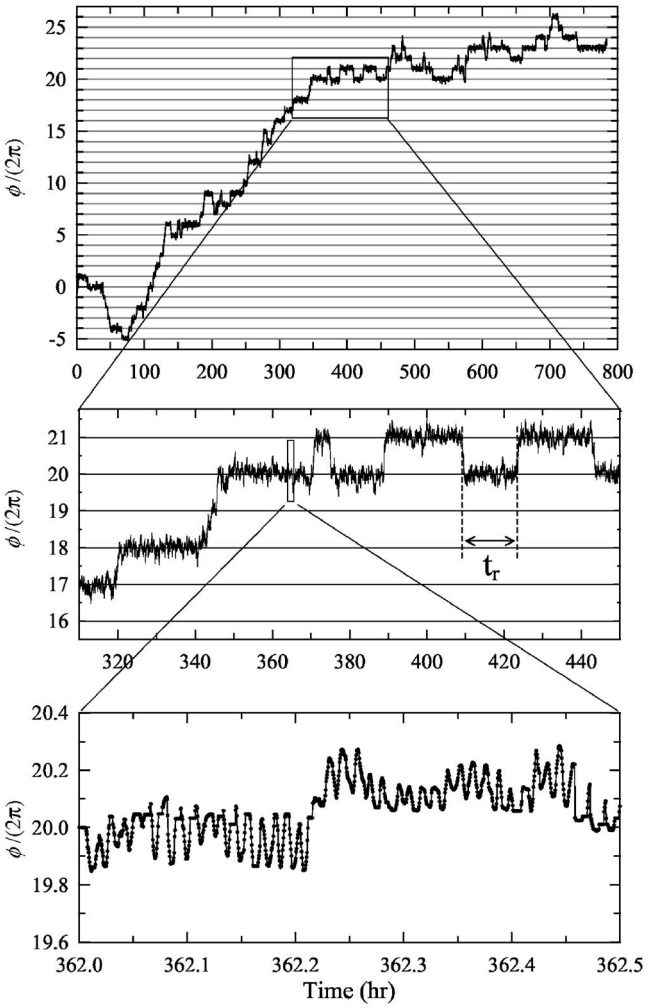


FIG. 18. Time trace of the azimuthal orientation angle $\phi(t)$ (in units of $2\pi$) of the mean wind measured in the flow-visualization experiment. From top to bottom: the entire trace of 783 h; a segment of 146 h; and a segment of 50 min.

### D. The residence property

We present in this subsection results from the long-time flow visualization measurement which is denoted as run no. 7, and its Ra and Pr are also listed in Table I. The data acquisition lasted for 33 days and the processed video recording of the flow indicator produced a quantitative measure of the azimuthal angle $\phi$ of the wind. The upper panel of Fig. 18 shows the entire trace of $\phi(t)$ over 783 h, with the middle and lower panels showing parts of it on expanded time scales. It is seen that this result, obtained using a different technique and near the bottom plate of the cell, exhibits similar features as those obtained using the PIV method near the top plate of the sapphire cell, i.e., the mean wind fluctuates around a preferred direction with both erratic and periodic oscillations over different time scales. It also exhibits net rotation and "residence" (or "locking") behavior. It is interesting to note from the trace that the mean wind shows a clockwise net rotation during the first 70 h or so (which is similar to the PIV results), changed to a counterclockwise rotation afterward, and then appeared to have leveled off for

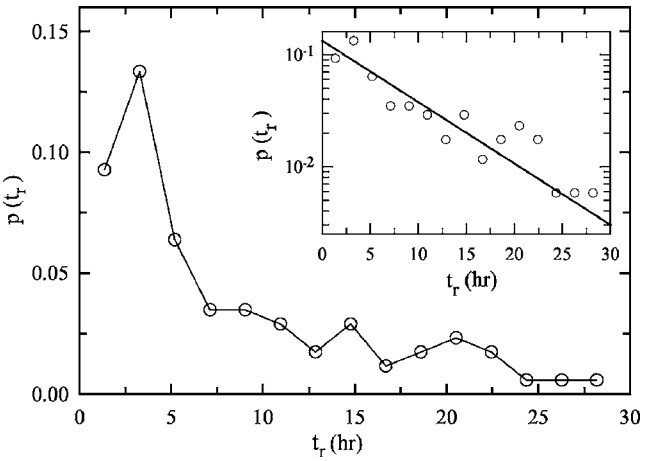


FIG. 19. Probability density function of the residence time $t_r$. Inset: the PDF of $t_r$ plotted in semi-logarithmic scale. See text for the explanation for the solid line.

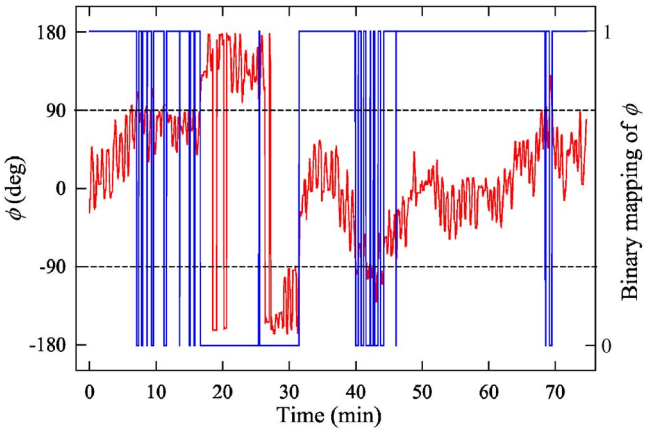


FIG. 20. (Color online) A segment of the time trace of $\phi$ (red curve) and its corresponding binary mapping (blue line).

the last 200 h. We do not know the reason for this change in the long-term trend with respect to net rotation, but it does not seem to have significant bearing on the statistical properties to be discussed in this and in the next section.

With the much longer time series we can examine some of the features of the wind's motion with better statistics. One of these is the "residence" property of the wind, i.e., its tendency to stay in a preferred direction with all other directions corresponding to "transient states." To characterize this "locking" behavior, we define $t_r$ as the time interval in which the wind resides in the "stable state" between two consecutive 360° turns [see Fig. 18(b)]. Borrowing a terminology from geomagnetism [57] we call $t_r$ the residence time, although in the geomagnetic context the transitions between consecutive residences are between two states.

A total of 90 residences are identified from the time series and the corresponding residence time $t_r$ ranges from 0.4 to 29 h. The average residence time is about 490 min, while the average transition time between consecutive residences is about 17 min. These features are very similar to those found from the records of geomagnetic reversals [57]. The PDF of $t_r$ is shown in Fig. 19 and the inset shows a semi-logarithmic plot of $p(t_r)$. It is seen that despite the very long time record there is still considerable scatter in the data; nevertheless, the general trend of an approximately exponential decay can be identified. In a recent model study of the reversal phenomenon in turbulent flows, Benzi [60] has found that the time interval (called the "exit time" in his paper but denoted here also as $t_r$) between transitions in two stable states has an exponential distribution, i.e., $p(t_r) = \langle t_r \rangle^{-1} \exp(-t_r/\langle t_r \rangle)$. This result is shown as the solid line in the inset of Fig. 19, where $\langle t_r \rangle \approx 8$ h for our data has been used. Since in our case there is only one "stable state," this result suggests that exponential distribution of the residence time may be a generic feature for these stochastic processes.

### E. Statistical properties of reversals

Several experiments have indicated that the mean wind in the horizontal plane is a band with a width of approximately half of the cell diameter [41,64]. Thus, each time the azimuthal orientation of the wind changes more than 90° the vertical component of the wind velocity measured near the sidewall will reverse its direction. With this understanding, we define a reversal event whenever the azimuthal angle of the wind crosses an angle orthogonal to the preferred angle. From the measured time series of $\phi$ over 33 days, about 22 000 reversals are identified by this method. It is interesting to note that the above identification of a reversal event amounts to a mapping of the time trace $\phi(t)$ to a "binary sequence." This is illustrated in Fig. 20 in which a segment of the measured trace (red) is shown along with the binary mapping (blue). In the figure $\phi$ has been shifted to within −180° to 180° and the preferred angle is set to 0. In this way, when $\phi(t)$ is within the angular range between −90° and 90°, the value of the mapping is set to 1; when $\phi(t)$ is outside the above range, the wind velocity near the sidewall switches direction and the mapping is set to 0. It should be stressed that the "reversal" events defined this way are not necessarily the same as those described by Sreenivasan *et al.* [54], in which a "reversal" is taken to be either a 180° azimuthal rotation or a cessation-led in-plane reversal of the wind, with the latter scenario favored by those authors. Nevertheless, as we shall see below the reversal properties from our data are similar to those found in [54]. It should be mentioned that similar identification of "reversals" from the measured $\phi(t)$ has also been used by Brown *et al.* [51] and that a similar method to discretize measured time series has been used previously by Bershadskii *et al.* [69] to study the phenomenon of plume clustering from the local temperature trace.

Similar to [54], we define $T_n$ as the time that the $n$th reversal, or transition between 0 and 1 of the binary mapping, occurred, with the time origin taken to be the start of the experiment. Figure 21 plots $T_n$ vs $n$, which shows an approximate linear relationship, which suggests stationarity in $T_n$ with the slope a measure of the mean time between reversals. The inset of Fig. 21 shows the deviation of $T_n$ from its linear trend. Similarly, as in [54], the detrended $T_n$ show characteristics of a Brownian process, i.e., a −2 slope of the power spectra and normality of the PDF, which are shown in Fig. 22. If we define $t_1$ as the time interval between adjacent reversals, i.e., $t_1 = T_{n+1} - T_n$, then $t_1$ also exhibits power-law

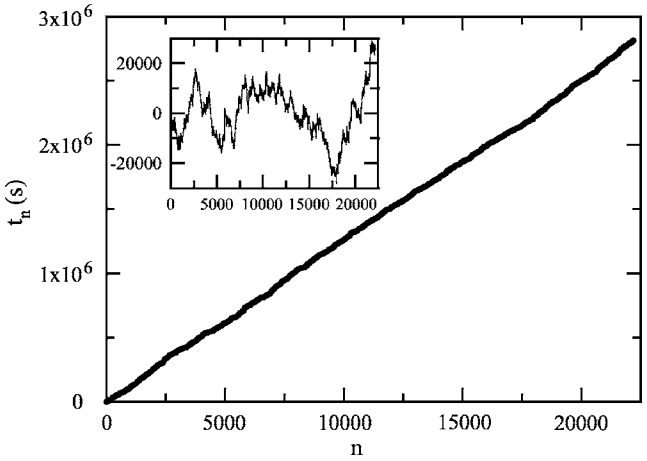


FIG. 21. The time of $n$th "reversal" $T_n$ as a function of $n$. Inset: detrended $T_n$ vs $n$.

decay for small values and exponential decay for larger values, which have been found previously [51,54]. Figures 23(a) and 23(b) plot the PDF of $t_1$ in log-log and semi-log scales, respectively. Note that the horizontal axes are normalized by the mean value $\langle t_1 \rangle = 126.6$ (s) $\approx 2.8\tau_o$. Although the power-law region in Fig. 23(a) is only about a decade, as is done in [54] the existence of a close-to $-1$ power-law decay may be confirmed by the existence of a logarithmic behavior of the cumulative PDF of $t_1$ over the same interval in $t_1$. In the inset of Fig. 23(a) the cumulative PDF $P(t)$ is plotted in semi-log scale showing this is indeed the case. The solid line in Fig. 23(b) is an exponential fit $p(t_1) \sim \exp[-t_1/(19.4\langle t_1 \rangle)]$ to the data points in the region and produces a characteristic decay time $t_{\exp} = 19.4\langle t_1 \rangle \approx 2450$ (s). It should be noted that the qualitative behavior for the distribution of $t_1$ has also been observed by Brown *et al.* [70]. While the exponent ($\sim -1.1$) of the power-law is close to that found in [54], the characteristic exponential decay time $t_{\exp}$ is rather different in the two cases, which is 400 s in [54]. In terms of the wind oscillation or circulation time $\tau_o$, in our case $t_{\exp} \approx 55\tau_o$ and it is $13\tau_o$ in [54]. In their physical model for the

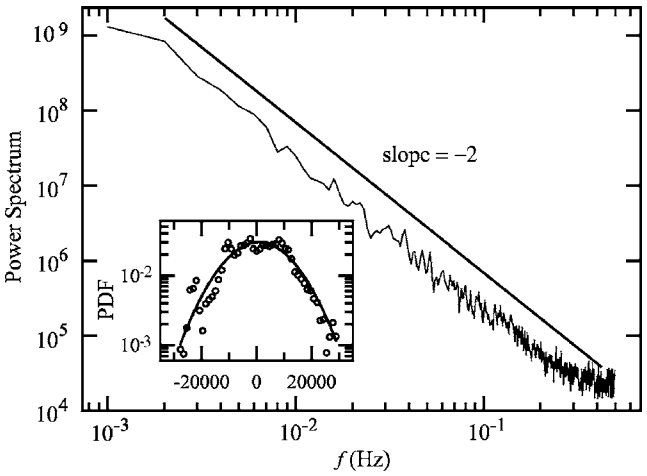


FIG. 22. Power spectrum density of the detrended $T_n$. Inset: the PDF of detrended $T_n$, the solid line is a Gaussian fit.

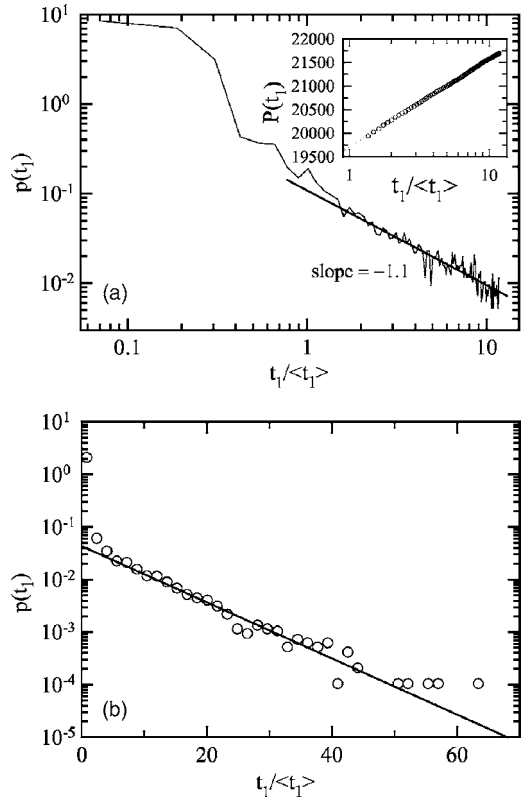


FIG. 23. (a) PDF of $t_1$ in log-log scale for small $t_1$. Inset: the corresponding cumulative distribution $P(t_1)$; the data can be excellently fitted to a straight line. (b) PDF of $t_1$ for larger values plotted in semi-logarithmic scale, the straight line indicates an exponential distribution of $t_1$.

reversal phenomenon, Sreenivasan *et al.* interpreted $t_{\exp}$ as the sidewall thermal equilibration time with an unusually hot/cold fluid parcel [54]. In the model estimation, $t_{\exp}$ is proportional to the thickness of the thermal boundary layer at the sidewall $\delta_{th,side}$, which has not been measured for water to the best of our knowledge. Using the previously measured [12] sidewall viscous boundary layer thickness $\delta_{v,side}$ instead, we estimate that the sidewall thermal equilibration time for our system should be $\approx 50$ (s). Because the viscous boundary layer thickness should always be larger than the thermal boundary layer thickness for sufficiently large Pr (which is the case for water), our estimation of the sidewall thermal equilibration time should be an upper bound. Note, however, that this result does not necessarily make any implication on the model itself, since, as already noted, the two cases may not study exactly the same phenomenon. If this is the case, then it suggests that both types of phenomena have the same qualitative properties and may have the same stochastic origin. In other words, the power-law decay in short time scales and exponential decay in long time scales is a rather robust feature of the underlying dynamics.

## IV. CONCLUSION

In conclusion, we have made direct measurement of the azimuthal motion of the wind in turbulent thermal convec-

tion. Using the PIV technique, both the azimuthal angle and the speed of the wind are obtained. In addition, the azimuthal orientation of the mean wind is measured separately by a visualization method over much longer time period. Both measurements give the same results.

A surprise finding of the experiment is that not only the orientation of the wind has a preferred direction in an apparatus with apparent cylindrical symmetry, as already observed previously [41,51], but that it is "locked" in the preferred direction with all other orientations appear as "transient states." That is, the azimuthal angle fluctuates about the preferred direction most of the time ($>90\%$) and large excursions often result in a net rotation that takes the wind back to the preferred orientation. It is also found that the preferred direction changes from run to run with no apparent trend. The experiment reveals that the rate of erratic rotation of the circulation plane of the wind, as measured by the rms increment of the azimuthal angle, has a strong dependence on Ra; it increases almost tenfold as Ra varied from $1\times10^9$ to $1\times10^{10}$. When the trend of net rotation is removed, it is found that the azimuthal motion consists of erratic fluctuations and a time-periodic oscillation. The amplitude of the periodic oscillation is found to have a nearly normal distribution, while the distribution for the amplitude of the erratic fluctuations deviates from normality with exponential tails. Both rotation-led and cessation-led flow reversals are observed, with the latter type of events much rarer than the former, which is in agreement with previous findings [51]. In addition, a "double-cessation" phenomenon has been observed. It is found that the azimuthal rotation rate of the wind and the magnitude of wind velocity (the wind speed) correlate negatively but within experimental uncertainty there is no significant phase difference between the two quantities. Our results also suggest that the oscillatory motion of the wind in its vertically oriented circulation plane, which is caused by the synchronized emission of plumes [39,41], and the orientational oscillation of the circulation plane itself have the same dynamic origin. We also found that the residence time, or the time the wind's orientation spent in the locked state, has an exponential distribution and its statistical properties resemble those of geomagnetic reversals. It is also found that rotations of the wind's circulation plane that result in flow reversals near the sidewall exhibit power-law distribution with a $-1$ slope in short time scales (several tens of circulation time) and exponential distribution in longer time scales.

## ACKNOWLEDGMENTS

It is a pleasure to acknowledge stimulating discussions with G. Ahlers. We also thank him and J. J. Niemela and K. R. Sreenivasan for their helpful comments on the preprint of this paper. Support of this work by the Research Grants Council of Hong Kong SAR under Project No. CUHK403003 is gratefully acknowledged.

[1] E. D. Sigga, Annu. Rev. Fluid Mech. **26**, 137 (1994).
[2] L. P. Kadanoff, Phys. Today **54**(8), 34 (2001).
[3] R. Krishnamurti and L. N. Howard, Proc. Natl. Acad. Sci. U.S.A. **78**, 1981 (1981).
[4] M. Sano, X.-Z. Wu, and A. Libchaber, Phys. Rev. A **40**, 6421 (1989).
[5] B. Castaing, G. Gunaratne, F. Heslot, L. Kadanoff, A. Libchaber, S. Thomae, X.-Z. Wu, S. Zaleski, and G. Zanetti, J. Fluid Mech. **204**, 1 (1989).
[6] A. Tilgner, A. Belmonte, and A. Libchaber, Phys. Rev. E **47**, R2253 (1993).
[7] A. Belmonte, A. Tilgner, and A. Libchaber, Phys. Rev. E **50**, 269 (1994).
[8] Y.-B. Xin, K.-Q. Xia, and P. Tong, Phys. Rev. Lett. **77**, 1266 (1996).
[9] R. M. Kerr, J. Fluid Mech. **310**, 139 (1996).
[10] Y.-B. Xin and K.-Q. Xia, Phys. Rev. E **56**, 3010 (1997).
[11] X. Chavanne, F. Chillà, B. Castaing, B. Hébral, B. Chabaud, and J. Chaussy, Phys. Rev. Lett. **79**, 3648 (1997).
[12] X.-L. Qiu and K.-Q. Xia, Phys. Rev. E **58**, 486 (1998).
[13] X.-L. Qiu and K.-Q. Xia, Phys. Rev. E **58**, 5816 (1998).
[14] S. Ashkenazi and V. Steinberg, Phys. Rev. Lett. **83**, 3641 (1999).
[15] K.-Q. Xia and S.-Q. Zhou, Physica A **288**, 308 (2000).
[16] S.-Q. Zhou and K.-Q. Xia, Phys. Rev. E **63**, 046308 (2001).
[17] R. D. Puits, C. Resagk, A. Tilgner, F. H. Busse, and A. Thess (unpublished).
[18] X.-L. Qiu, K.-Q. Xia, and P. Tong, J. Turbul. **6**, 1 (2005).
[19] A. M. Garon and R. J. Goldstein, Phys. Fluids **16**, 1818 (1973).
[20] K. Tanaka and H. Miyata, Int. J. Heat Mass Transfer **23**, 1273 (1980).
[21] B. I. Shraiman and E. D. Siggia, Phys. Rev. A **42**, 3650 (1990).
[22] T. Takeshita, T. Segawa, J. A. Glazier, and M. Sano, Phys. Rev. Lett. **76**, 1465 (1996).
[23] S. Grossmann and D. Lohse, J. Fluid Mech. **407**, 27 (2000).
[24] Z. A. Daya and R. E. Ecke, Phys. Rev. Lett. **87**, 184501 (2001).
[25] X. Chavanne, F. Chillà, B. Chabaud, B. Castaing, and B. Hébral, Phys. Fluids **13**, 1300 (2001).
[26] S. Lam, X.-D. Shang, S.-Q. Zhou, and K.-Q. Xia, Phys. Rev. E **65**, 066306 (2002).
[27] S. Grossmann and D. Lohse, Phys. Rev. E **66**, 016305 (2002).
[28] S. Grossmann and D. Lohse, J. Fluid Mech. **486**, 105 (2003).
[29] C. Sun and K.-Q. Xia, Phys. Rev. E **72**, 067302 (2005).
[30] S. Ciliberto, S. Cioni, and C. Laroche, Phys. Rev. E **54**, R5901 (1996).
[31] S. Cioni, S. Ciliberto, and J. Sommeria, J. Fluid Mech. **335**, 111 (1997).
[32] X.-L. Qiu, S. H. Yao, and P. Tong, Phys. Rev. E **61**, R6075 (2000).
[33] E. S. C. Ching and K. F. Lo, Phys. Rev. E **64**, 046302 (2001).
[34] X.-L. Qiu and P. Tong, Phys. Rev. E **64**, 036304 (2001).

[35] S. Kenjereš and K. Hanjalić, Phys. Rev. E **66**, 036307 (2002).
[36] R. Verzicco and R. Camussi, J. Fluid Mech. **477**, 19 (2003).
[37] K.-Q. Xia, C. Sun, and S.-Q. Zhou, Phys. Rev. E **68**, 066303 (2003).
[38] J. J. Niemela and K. R. Sreenivasan, Europhys. Lett. **62**, 829 (2003).
[39] X.-L. Qiu, X.-D. Shang, P. Tong, and K.-Q. Xia, Phys. Fluids **16**, 412 (2004).
[40] M. Breuer, S. Wessling, J. Schmalzl, and U. Hansen, Phys. Rev. E **69**, 026302 (2004).
[41] C. Sun, K.-Q. Xia, and P. Tong, Phys. Rev. E **72**, 026302 (2005).
[42] C. Sun, H.-D. Xi, and K.-Q. Xia, Phys. Rev. Lett. **95**, 074502 (2005).
[43] Y. Tsuji, T. Mizuno, T. Mashiko, and M. Sano, Phys. Rev. Lett. **94**, 034501 (2005).
[44] T. Haramina and A. Tilgner, Phys. Rev. E **69**, 056306 (2004).
[45] A. Parodi, J. von Hardenberg, G. Passoni, A. Provenzale, and E. A. Spiegel, Phys. Rev. Lett. **92**, 194503 (2004).
[46] U. Burr, W. Kinzelbach, and A. Tsinober, Phys. Fluids **15**, 2313 (2003).
[47] E. Calzavarini, D. Lohse, F. Toschi, and R. Tripiccione, Phys. Fluids **17**, 055107 (2005).
[48] G. Zocchi, E. Moses, and A. Libchaber, Physica A **166**, 387 (1990).
[49] E. Villermaux, Phys. Rev. Lett. **75**, 4618 (1995).
[50] H.-D. Xi, S. Lam, and K.-Q. Xia, J. Fluid Mech. **503**, 47 (2004).
[51] E. Brown, A. Nikolaenko, and G. Ahlers, Phys. Rev. Lett. **95**, 084503 (2005).
[52] G. Ahlers, E. Brown, and A. Nikolaenko, J. Fluid Mech. **557**, 341 (2006).
[53] J. J. Niemela, L. Skrbek, K. R. Sreenivasan, and R. J. Donnelly, J. Fluid Mech. **449**, 169 (2001).
[54] K. R. Sreenivasan, A. Bershadskii, and J. J. Niemela, Phys. Rev. E **65**, 056306 (2002).
[55] J. J. Niemela and K. R. Sreenivasan, Physica A **315**, 203 (2002).
[56] G. A. Glatzmaier, R. S. Coe, L. Hongre, and P. H. Roberts, Nature (London) **401**(6756), 885 (1999).
[57] G. Consolini and P. De Michelis, Phys. Rev. Lett. **90**, 058501 (2003).
[58] E. van Doorn, B. Dhruva, K. Sreenivasan, and V. Cassella, Phys. Fluids **12**, 1529 (2000).
[59] U. Hansen, D. A. Yuen, and S. E. Kroening, Geophys. Astrophys. Fluid Dyn. **63**, 67 (1991).
[60] R. Benzi, Phys. Rev. Lett. **95**, 024502 (2005).
[61] F. F. Araujo, S. Grossmann, and D. Lohse, Phys. Rev. Lett. **95**, 084502 (2005).
[62] R. C. Hwa, C. B. Yang, S. Bershadskii, J. J. Niemela, and K. R. Sreenivasan, Phys. Rev. E **72**, 066308 (2005).
[63] D. Funfschilling and G. Ahlers, Phys. Rev. Lett. **92**, 194502 (2004).
[64] S.-L. Lui and K.-Q. Xia, Phys. Rev. E **57**, 5494 (1998).
[65] R. J. Adrian, Annu. Rev. Fluid Mech. **23**, 261 (1991).
[66] X.-L. Qiu and P. Tong, Phys. Rev. E **66**, 026308 (2002).
[67] X.-D. Shang and K.-Q. Xia, Phys. Rev. E **64**, 065301(R) (2001).
[68] J. Zhang, S. Childress, and A. Libchaber, Phys. Fluids **9**, 1034 (1997).
[69] A. Bershadskii, J. J. Niemela, A. Praskovsky, and K. R. Sreenivasan, Phys. Rev. E **69**, 056314 (2004).
[70] G. Ahlers (private communication).